CORA Cork Open Research Archive
Cartlann Taighde Oscailte Chorcaí

Title	Quantum confined intense red luminescence from large area monolithic arrays of mesoporous and nanocrystal-decorated silicon nanowires for luminescent devices
Authors	O'Dwyer, Colm;McSweeney, William;Collins, Gillian
Publication date	42248
Original Citation	O'Dwyer, C., McSweeney, W. and Collins, G. (2016) 'Quantum Confined Intense Red Luminescence from Large Area Monolithic Arrays of Mesoporous and Nanocrystal-Decorated Silicon Nanowires for Luminescent Devices', ECS Journal of Solid State Science and Technology, 5(1), pp. R3059-R3066. doi: 10.1149/2.0081601jss
Type of publication	Article (peer-reviewed)
Link to publisher's version	http://jss.ecsdl.org/content/5/1/R3059.abstract?cpetoc - 10.1149/2.0081601jss
Rights	© The Author(s) 2015. Published by ECS. This is an open access article distributed under the terms of the Creative Commons Attribution 4.0 License (CC BY, http://creativecommons.org/licenses/by/4.0/), which permits unrestricted reuse of the work in any medium, provided the original work is properly cited. - https://creativecommons.org/licenses/by/4.0/
Download date	2026-11-06 09:55:48
Item downloaded from	https://hdl.handle.net/10468/6054

UCC
University College Cork, Ireland
Coláiste na hOllscoile Corcaigh

JSS Focus Issue on Novel Applications of Luminescent Optical Materials

Quantum Confined Intense Red Luminescence from Large Area Monolithic Arrays of Mesoporous and Nanocrystal-Decorated Silicon Nanowires for Luminescent Devices

Colm O'Dwyer,[a,b,*,z] William McSweeney,[a] and Gillian Collins[a,c]

[a]*Department of Chemistry, University College Cork, Cork, T12 YN60, Ireland*
[b]*Micro-Nano Systems Centre, Tyndall National Institute, Lee Maltings, Cork, T12 R5CP, Ireland*
[c]*AMBER@CRANN, Trinity College Dublin, Dublin 2, D02 PN40, Ireland*

We report intense red luminescence from mesoporous n^+-Si(100) nanowires (NWs) and nanocrystal-decorated p-Si NWs fabricated using electroless metal assisted chemical (MAC) etching. n^+-Si NWs are composed of a labyrinthine network of silicon nanocrystals in a random mesoporous structure. p-type Si(100) NWs exhibit solid core structure, with a surface roughness that contains surface-bound nanocrystals. Both mesoporous n^+-Si NWs and rough, solid p-Si NWs exhibit red luminescence at ∼1.7 and ∼1.8 eV, respectively. Time-resolved photoluminescence (PL) measurements indicated long (tens of μs) radiative recombination lifetimes. The red luminescence is visible with the naked eye and the red light is most intense from mesoporous n^+-Si NWs, which exhibit a red-shift in the emission maximum to 1.76 eV at 100 K. The red PL from monolithic arrays of p-type NWs with nanocrystal-decorated rough surfaces is comparatively weak, but originates from the surface bound nanocrystals. Significant PL intensity increase is found during excitation for mesoporous NWs. X-ray photoelectron spectroscopy identifies a stoichiometric SiO_2 on the rough p-Si NWs with a SiO_x species at the NW surface. No distinct oxide is found on the mesoporous NWs. The analysis confirms that long life-time PL emission arises from quantum confinement from internal nanoscale crystallites, and oxidized surface-bound crystallites, on n^+- and p-Si NWs respectively.
© The Author(s) 2015. Published by ECS. This is an open access article distributed under the terms of the Creative Commons Attribution 4.0 License (CC BY, http://creativecommons.org/licenses/by/4.0/), which permits unrestricted reuse of the work in any medium, provided the original work is properly cited. [DOI: 10.1149/2.0081601jss] All rights reserved.

Manuscript submitted June 16, 2015; revised manuscript received August 11, 2015. Published September 1, 2015. *This paper is part of the JSS Focus Issue on Novel Applications of Luminescent Optical Materials.*

Recent advancements in the growth and formation of semiconducting nanostructures, particularly group 14 metalloid semiconductors such as silicon and germanium have shown how quantum effects can be engineered and controlled[1–3] to modify thermal and optical properties.[4,5] In particular, the nanostructuring of silicon materials mediates phonon scattering and confinement, including reduction of thermal conductivity[6–9] and Si-based nanowire heterostructures have been employed as solar cell materials and nanoelectronic power sources.[10] Crystal sizes below the Bohr radius also results in light emission, and effective bandgap modification can influence absorbed thermopower in nanoscale silicon, and for photovoltaics.[11] In photovoltaics, polycrystalline silicon comprises more than 90% of the PV cell production. The efficiency is limited to ∼33–35%, with most of the power converted to heat via phonon emission.[12] Recent developments in nanoscale silicon crystals that provide multiple exciton generation events (at energies greater than twice the bandgap) per incident photon may improve efficiencies.[13]

Porous semiconductors and clusters of quantum dots, particularly of silicon, have also been the subject of intense research recently for Li-ion batteries[14–16] water oxidation[17] and electroluminescent devices[18] and those exhibiting optical gain,[19–21] and a range of (bio)sensors.[22,23] Since the discovery of visible light emission in porous silicon[24–26] that in the main, arose from quantum confinement effects, porous silicon has had some usefulness for nanoelectronic devices,[27] and field effect transistors.[28] Single-pass optical gain in nanoscale silicon reported in 2000 proved to be limited by free carrier absorption (FCA),[29,30] and even with increased optical pump powers, the FCA mechanism normally offsets gain from the nanocrystals, preventing possibilities for silicon lasing for instance. Nanocrystals and quantum dots of silicon have shown promise for nano-lasers.[31] Since then, significant efforts have been made to engineer the structures of nanoscale silicon, beginning either electrochemical etching,[32,33] through to nanoelectronics top-down processing. Top-down porous silicon formation, if controlled, allows monolithic nanoscale silicon array formation directly on device compatible wafers, where the doping density is predefined during silicon crystal growth. While bottom-up vapor-liquid-solid (VLS) wires can be grown in high yield, the presence of non-radiative and other recombination centers,[34] and from metal atom incorporation from the catalyst during growth[35,36] influence light emission characteristics. The difficulty in controlling NW widths below the Bohr radius length scale, means that intense light emission is difficult to realize in NW systems without control of radiative defects or formation of internal, smaller length scale crystallites to confine photons and provide efficient exciton generation. Efforts to control light emission from silicon NWs have demonstrated co-existence of 1D and quasi-0D photoluminescence in single NWs.[37]

Electroless etching protocols that use Ag^+ at the silicon surface with subsequent silicon oxidation and dissolution in HF, has proven to be useful in forming arrays of Si NWs.[38-40] Si NWs can developed significant roughness under these etching conditions,[41] but when an n-type semiconductor-solution interface is biased electrolessly via the potential difference between the redox even of Ag^+ reduction and the Si Fermi level, significant charge transfer can occur, limited by a very thin depletion region in highly doped n-type materials resulting in internal mesoporosity formation within the NWs.[42–46] Controlling the internal crystal density and overall structure through electrochemically formed porosity is useful for large area surface modification of silicon,[47] and can in some cases, avoid the need for complex intermediate steps to promote consistent or ordered surface assembly. These methods often require organic ligands, control of surface wetting and nanocrystal interaction forces to maximize packing to create uniform areal density deposition at device-scale areas. The removal of the organic species needed for optoelectronic device applications can perturb these assemblies. The development of top-down approaches for etching semiconductors,[48,49] particularly for nano-silicon that avoids organic species and allows a defined doping density and type, is useful for luminescent devices. Oxidation routes are possible too, but oxide formation has implications for electroluminescent devices. Aside from recombination effects in SiO_2 and in organic ligand inter-crystal layers, the electrical contact resistance is worsened. Internal mesoporosity potentially allows for tunability in the photo or electroluminescence of silicon from silicon wafers.

*Electrochemical Society Active Member.
[z]E-mail: c.odwyer@ucc.ie

Downloaded on 2015-09-01 to IP 93.94.208.154 address. Redistribution subject to ECS terms of use (see ecsdl.org/site/terms_use) unless CC License in place (see abstract).

Here, we demonstrate intense red luminescence from silicon NWs formed as monolithic arrays of either internally mesoporous NWs, or solid-core nanocrystal-decorated NWs with doping type and carrier concentration of the parent wafer. In n^+-Si NWs, internal mesoporosity facilitated by enhanced, but space charge-limited etching in all directions, results in NWs that are entirely porous comprising bridged nanocrystals in each NW within the monolithic NW layer. Both nanocrystal-decorated p-Si NWs and n^+-Si NWs are shown to emit visible red light and 1.8 and 1.7 eV, respectively. For (electro)luminescent devices, the intense red light emission energy and intensity is tunable with temperature. The analysis confirms that PL emission arises predominantly from quantum confinement from internal nanoscale crystallites within n^+-Si NWs and oxidized surface-bound crystallites on p-Si NWs.

Experimental

100 mm p-type B-doped Si(100) wafers (365 μm thickness) with a resistivity of 1–30 $\Omega \cdot$cm corresponding to a doping density of between 1.6–7.0 $\times$ 10^{14} cm^{-3}, and n-type Si(100) wafers, As-doped with resistivity in the range 0.001–0.005 $\Omega \cdot$cm corresponding to a doping density of between 1.2 – 7.4 $\times$ 10^{19} cm^{-3}, were used. The substrates were etched by immersion in a 50 °C thermostated solution of 10% HF containing 0.02 mol dm^{-3} $AgNO_3$ for 1 h. After etching NW layers were washed copiously with deionized water and concentrated nitric acid to completely remove remnant Ag deposits.

Scanning electron microscopy (SEM) were acquired using a Hitachi S4800 FESEM operating at 5–10 kV. Transmission electron microscopy (TEM) was conducted at 200 kV using a JEOL TEM JEM-2100. Scanning TEM and bright field high angle annular dark field (HAADF) imaging was acquired using a JEOL JEM-2100F FEGTEM at 200 kV.

Photoluminescence (PL) were acquired using an excitation provided by a 325 nm emission from a cw He-Cd laser with maximum power density of 2 W/cm^2. Optical images of red luminescence Si NW layers were acquired by illuminating sample with the He-Cd beam through a lens under complete defocus to ensure near-uniform illumination flood. PL spectra were acquired using a Horiba iHR320 spectrometer equipped with a Synapse CCD matrix. Samples were placed in an evacuated chamber of a Janis closed-cycle helium cryostat for temperature-dependent PL measurements. PL spectra were thus acquired from room temperature (300 K) down to 100 K. Time-resolved measurements of PL decay were acquired at 725 nm for n^+-Si NWs and at 685 nm for p-Si NWs after steady state pumping.

For higher power excitation the attenuation and focusing resulted in an excitation intensity in the range 0.2–2000 W/cm^2. Luminescence is collected with a $f = 60$ mm achromat and a high-pass filter (Schott OG570) was used to suppress scattered excitation light. The luminescence was imaged onto the entrance slit of the 0.25 m spectrometer, with a time resolution of 50 ns.

Results and Discussion

Figures 1a and 1b shows electron microscopy images of the p-Si NW and n^+-Si NW monolithic arrays on Si(100) wafers. The NWs are formed in a remarkably dense array, with aspect ratios in this case are 1000–1200 (p) and ∼50–75 (n^+), respectively, and these can be tuned by varying etching conditions such as H_2O_2 and HF concentrations, temperature, time and $AgNO_3$ concentration.[50] Under the conditions outlined in the Experimental section, the TEM data in Fig. 1c show that n^+-Si NWs are composed of a random network of nanocrystallites of Si forming the internal mesoporosity. This mesoporous structure permeates the entire NW. This mesoporosity is believed to contribute to enhanced clumping due to evaporative drying from capillary forces, in spite of the mesoporous NWs being several times thicker than solid core p-type wires.

For the n^+-Si NWs, the mesoporosity in internal and nanocrystallites are internally bridged forming a network of random but equidistant (in 3D) nanocrystals defining maximum mesoporosity. Whereas

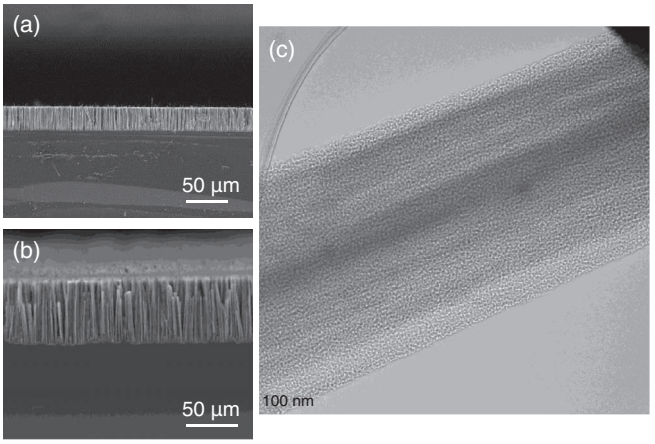


Figure 1. (a) SEM image of p-Si NW layers etched from Si(100) and (b) n^+-Si NW layer. (c) HRTEM image of a single n^+-Si NW of ∼600 nm diameter, with internal mesoporosity.

partial porosity in the form of etched holes (voids) has been reported in NWs, these NWs comprise a network of nanocrystals that extends self-similarly from the outer surface into the core. Specific details on the nature of the porous structure and surface roughness can be found elsewhere.[42] Highly mesoporous NWs appear semi-transparent to a 200 kV electron beam. The internal nanocrystal diameters forming the mesoporous structure range from 3–15 nm owing to the random nature of the galvanic displacement etching process, see Fig. 1c, and are thus amenable to quantum confinement (*vide infra*). Previous reports have suggested NW are formed with ∼7 nm diameters from this method,[51] and ascribe Raman shifts in TO phonon modes from these small diameters. Such low diameter NWs are rarely possible for the NWs by MAC etching – as shown here, the internal or surface features within or on the NW approach these sizes, not the NWs themselves.

The p-Si NWs, shown in Fig. 2a, maintain a solid crystalline core, aligned along the [100] direction. The sidewalls are rough, and such roughness has been shown to exhibit characteristic wavelengths,[9] with a higher degree of roughness characteristic of p-type Si(100) when its resistivity is reduced. p-Si NWs have diameters of ∼100 nm, typically 5–7× narrower than the wide n^+-Si NWs in Fig. 1c. As these NWs are too large as NW structures to cause quantum confinement, we examined the nature of the surface roughness by scanning TEM and high angle annular dark field (HAADF) methods. STEM avoids inaccuracies of roughness estimates in Si NW by TEM that are caused by viewing multiple roughness features that overlap in projection in through-focal TEM images.

Line profiles analysis of STEM data in the framework of standard rms roughness and correlation functions outlined elsewhere[52] for the p-Si NWs gives typical values of 1.8–2.2 nm with associated correlation lengths of 20–28 nm across the NW surface. For p-Si NWs on SS, the $K\alpha_1$ and $K\alpha_2$ lines are resolved in X-ray diffraction patterns (Fig. 1d), even for wires with diameters in the range 90–200 nm with solid cores. The corresponding patterns for mesoporous n^+-Si NWs (Fig. 1e) have much lower intensity convoluted high angle reflections. Estimate of average crystallite sizes within the mesoporous n^+-Si NWs from line broadening from the Scherrer relation is ∼12 nm, not accounting for residual tensile strain that may be present within NWs (compared to a bulk Si(100) wafer).

HRTEM analysis of the roughness features in Fig. 3 reveals that the outer edges are in fact an array of individual nanocrystalline regions with grain boundaries that are of sufficiently small size to contribute to quantum confined emission. The density of these surface-bound nanocrystals is much less that mesoporous n^+-Si NWs of course for a given areal density of NWs with equal length, but it is a confirmation that the surface features comprise the nanocrystallites of Si that provide a source of quantum confined visible red light emission from solid, rough Si NWs. Additionally, the observation of these

Downloaded on 2015-09-01 to IP 93.94.208.154 address. Redistribution subject to ECS terms of use (see ecsdl.org/site/terms_use) unless CC License in place (see abstract).

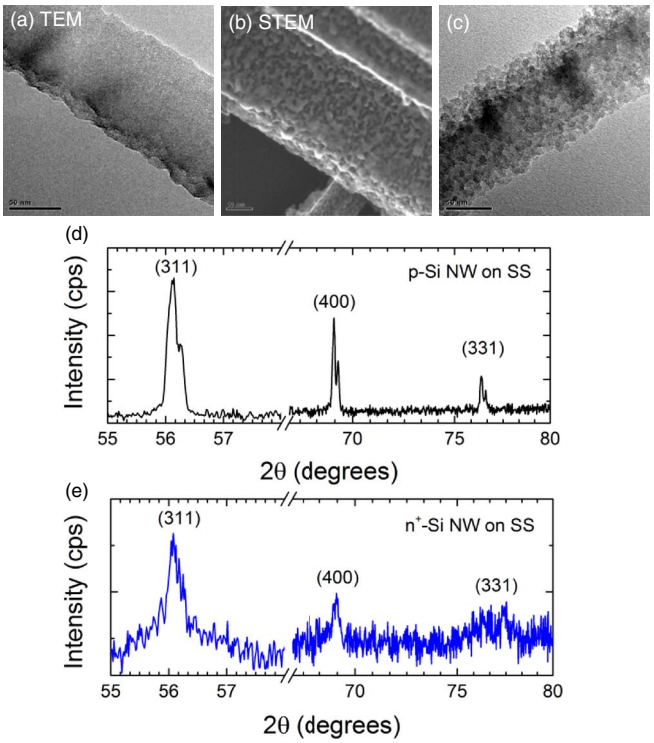


Figure 2. (a) TEM image of a single p-Si NW showing the solid core structure and the rough outer edges. (b) Bright field STEM secondary electron image of a p-Si NW showing the roughness development on the outer surface across the surface in the image plane. (c) TEM image of p-Si NW etched to exhibit highly developed surface roughness. (d,e) High angle XRD patterns showing (311), (400) and (331) reflections for p- and n^+-Si NWs.

crystallites may also help to explain phonon scattering mechanism in rough Si NWs, where the roughness boundary scattering of phonons cannot explain fully that observed degree of scattering.[9] Phonon confinement too (for acoustic phonons < 5 nm in wavelength), may also be influenced leading to electron-phonon interactions in solid NWs.

MAC etched Si-NW layer in monolithic form exhibit strong visible light scattering and mesoporous n^+-Si NW appear black as shown in Fig. 4a, while p-Si NW appear dark brown. Under flat-field excitation with a cw 385 nm laser at complete defocus, the NW array emits intense red luminescence as seen in the single-frame digital image in Fig. 4b.

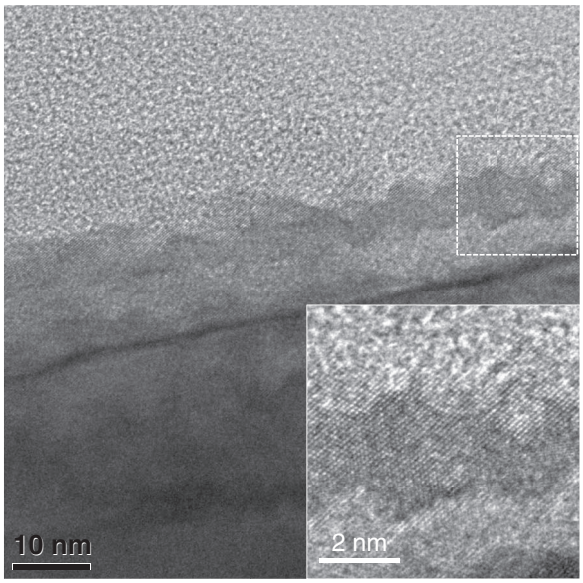


Figure 3. HRTEM evidence of the nanocrystal decoration of the outer rough edges of p-Si NWs.

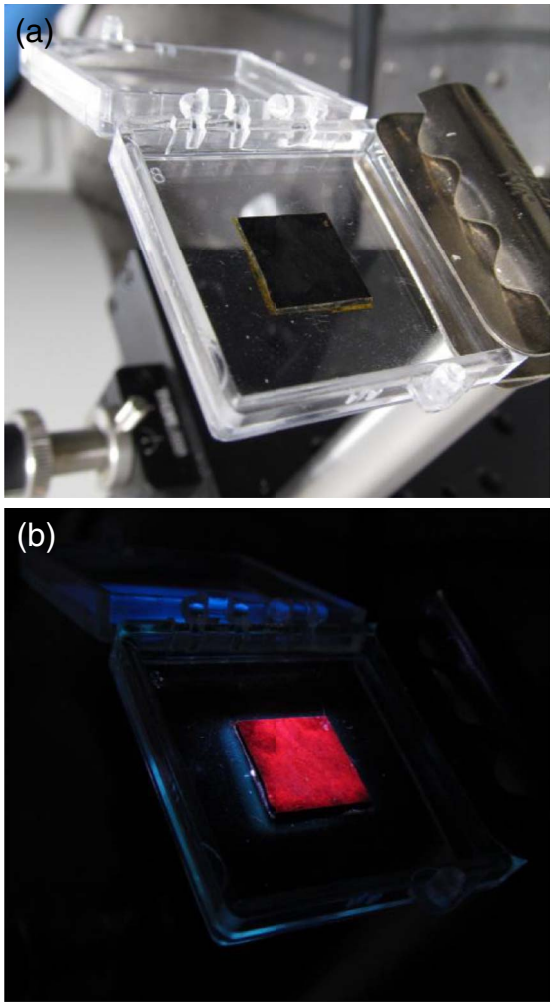


Figure 4. Photographs of n^+-Si NW array samples in (a) visible light and (b) in the dark under flat-field excitation with a 385 nm He-Cd laser. The NW layer appears black in visible light due to scattering. The red photoluminescence is visible to the naked eye.

Both n^+-Si NW and p-Si NW layers emit visible PL even though the p-Si NWs have solid cores and are 100–350 nm in diameter. The PL spectra are shown in Fig. 5a and demonstrate that both type of Si NW exhibit broadband emission with maxima at 685 nm and 720 nm for p- and n^+-Si NWs, with corresponding FWHM of 160 nm and 178 nm, respectively. These spectra were acquired several days after etching. The PL emission maxima are stable and do not shift with time. Time-resolved PL measurements of NW layers emitting intense red light at room temperature were also examined after the NWs were illumination continuously for several hours and the PL emission peak remained stable. The PL decay responses are shown in Fig. 5b and were acquired over a time period where PL intensity increase was negligible (a factor of 1.04 increase over 100 s). We find that exciton lifetimes from the mesoporous networked nanocrystal NWs and nanocrystal–decorated rough solid-core p-type NWs are up to several tens of μs, indicating effectively defect free, indirect gap nanocrystalline materials (defect free inside the nanocrystal). Indeed, quantum-confined emission to higher (blue) light form silicon nanocrystals has been reported due to traps from low-density nitrogen and oxygen impurities introduced during their synthesis, likely

Downloaded on 2015-09-01 to IP 93.94.208.154 address. Redistribution subject to ECS terms of use (see ecsdl.org/site/terms_use) unless CC License in place (see abstract).

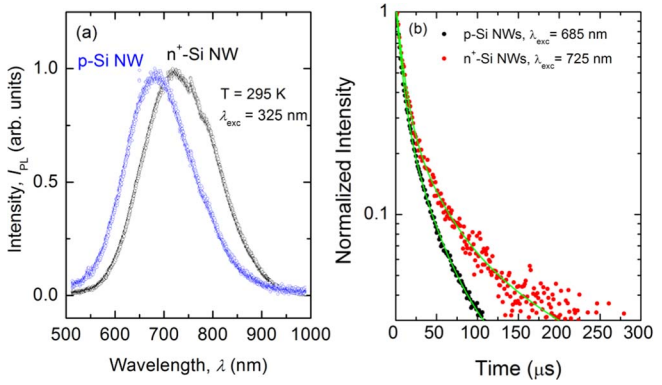


Figure 5. (a) Room-temperature photoluminescence spectra of n^+-Si NW and p-Si NW arrays. The intensity values are normalized. (b) Time-resolved PL measurements from both NW sample acquired at the peak PL emission energy for each NW type. The emission decay lifetimes are fitted using a bi-exponential.

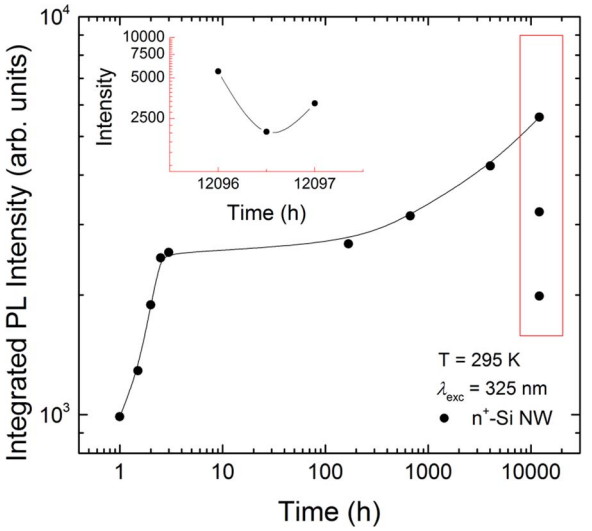


Figure 6. Integrated PL spectrum intensity for n^+-Si mesoporous NWs acquired over 3 h after etching, after 1 week, 1 month, 6 months, and 1.5 years. A second series of measurements were acquired for a period of 1 h after 1.5 years in ambient air. (Inset) zoom of the data points between 12096 and 12097 h).

from amino or related organic passivating of shape and size mediating surfactants[53] from solution-based colloidal synthesis methods.

These values are more than two orders of magnitude greater than emission lifetimes reported for lithographically structures NW pillar arrays. The spectra in Fig. 5 are free from excitonic transitions as the nanocrystalline content of the nanowires remain essentially as indirect gap semiconductors. We assume that there is no Stokes shift and that the effective bandgap is given by the PL emission maximum. Faster decay times caused by phonon-assisted recombination, which is more efficient at a given temperature for smaller crystallite sizes, are observed for the p-type Si NWs. These measurements are in agreement with microscopy and Raman data for the small crystallites decorating the surface of rough p-type etched Si NWs. It is important to note that strain and stress effect that are indicated by Raman shifts should not be automatically assigned to strain effects on the band structure and quantum confined emission variation. Phonon scattering by various mechanisms (boundary and Umklapp scattering) and confinement effects in mesoporous Si can also cause a Raman shift and asymmetry that is separate to strain relief.[9] While oxide-mediated defect states may contribute to a reduction in PL emission intensity or a red-shifting due to dominant excitation from lower energy transitions, the oxide in either type of NW is not a dominant contributory factor as the emission energies from p-type NWs are higher in energy than mesoporous n-type NWs, although with much lower intensity. The remnant Ag content was below 0.2%, confirmed by X-ray photoelectron spectroscopy.

The PL intensity at room temperature showed specific ageing increase based on individual measurements over a period of 1.5 years from the time of etching. Here, the measurement does not entirely account for processes relating to laser-induced adsorption/desorption of species such as oxide growth intermediates that affect radiative states at the silicon surface. In any case, the surface area in n^+-Si NWs is much greater than the p-Si NWs. Figure 6 shows the PL intensity maximum from each measurement over a 3 h period after etching, after 1 week in air, 6 months in air and again over a 3 h period after 1.5 ys in ambient environment.

The intensity values arise from the integrated PL obtained from an entire spectrum acquisition at $\lambda_{exc} = 325$ nm at each time step. Both types of NW show a consistent quasi-linear increase in intensity, with the n^+-Si NW intensity always greater. Ghosh et al.[54] also showed that PL intensity is a function of etching time in cases where nanocrystals are observed on the surface of the NW. The intensity saturates for the p-Si NWs after a week, with n^+-Si NWs exhibit a marked increase with time. The intensity decreases when left in air for 1.5 ys, but increases upon illumination again for a 1 h period for n^+-Si NWs, which do not actively grow oxides in time.

We do not observe strong emission from *e-h* plasma contributions from these monolithic NW arrays in the NIR region. Thus effective passivation of surface states that quenches non-radiative de-excitation modes is not confirmed here to be a significant contributory factor to mesoporous NW PL. No shift in the effective bandgap energy is found in time for these samples, but we do remark that in a fixed experiment, the intensity is a function of position on the sample, as the density of NW is not uniform in MAC etched NW arrays. We do not observe an intensity plateau for n^+-Si NWs, but if the effect is a function of surface area accessibility and scattering, we would expect that nanocrystal-decorated solid core NWs may plateau sooner than n^+-mesoporous Si NWs. Artoni et al.[51] showed that a vacuum can negate the effect of PL intensity increase in MACE Si-NWs with time, thus the effect is possibly a function of the nature of oxidizing species and surface area. We previously determined via HRTEM that the rough edges of the p-Si NWs are coated with a thin 1–3 nm SiO_2,[42] a stable a continuous oxide is formed after several days and does not thicken, thus low power lasers that do not affect this oxide layer may provide a definitive experiment to unequivocally determine the nature of PL increase at room temperature and effects of surface species desorption without competitive re-oxidation or laser-power induced localized heating.

XPS measurements were conducted on both NW types to determine the nature of the oxide species, which has been reported to contribute to PL emission processes involving *e-h* plasmas (but in the NIR energies), and blue luminescence from defects.[55,56] Figure 7a show the Si 2p core-level emission spectrum for p-Si NWs ~1 week after etching, and exhibit the hyperfine Si $2p_{3/2}$ and Si $2p_{3/2}$ from Si^0 in addition to two other oxidation states.

The measurements are consistent with a 1–3 nm oxide film coating the rough surface features, and confirms a predominantly stoichiometric SiO_2 coverage. Some sub-stoichiometric SiO_x ($x < 2$) is present. When the NW surface is sputtered with Ar^+, as shown in Fig. 7b, the amount of SiO_2 indicated by the integrated photoemission area, decreases while the relative amount of SiO_x increases. This confirms that the sub-oxide is located at the NW surface region. It is important to note that no coherent oxide film (with thickness >1 nm) is found around the nanocrystals that make up the internally mesoporous n^+-Si NWs, and they exhibit the most intense red light emission at room temperature. Previous reports on porous silicon have postulated that localized Si-O-Si-R (R = -OH, H) structures act as *e-h* radiative centers at the nanoscale silicon-pore interface (where the sub-oxide is located in the present case for p-NWs). Such a mechanism involves such polyatomic Si-O-Si-R structures and that radiative

Downloaded on 2015-09-01 to IP 93.94.208.154 address. Redistribution subject to ECS terms of use (see ecsdl.org/site/terms_use) unless CC License in place (see abstract).

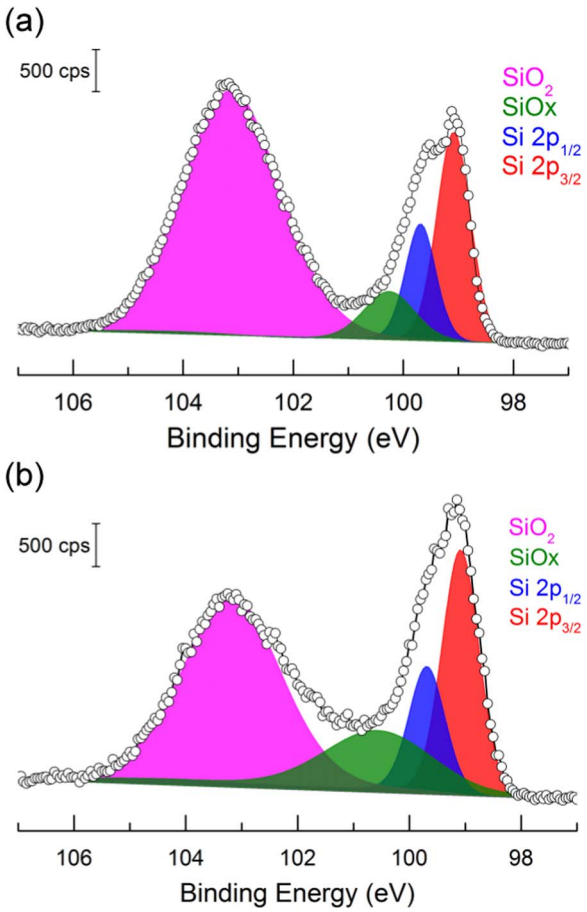


Figure 7. XPS Si 2p core-level photoemission spectra from (a) p-Si NWs after 1 week in ambient air and (b) after Ar^+ sputtering for 5 mins at 0.2 kV.

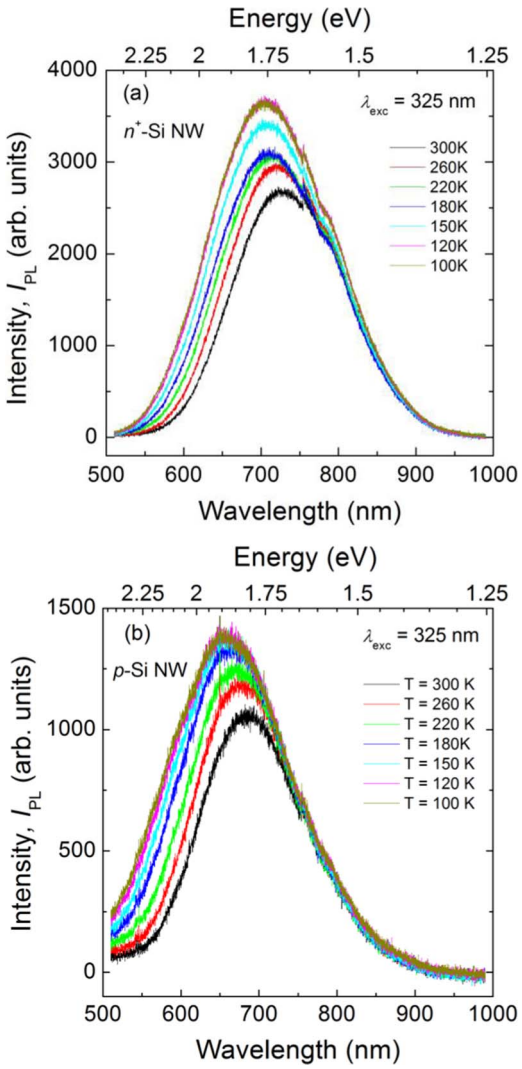


Figure 8. Photoluminescence spectra of (a) n^+-Si NW and (b) p-Si NW arrays acquired between T = 100–300 K. Excitation was provided by a cw He-Cd laser at 385 nm.

recombination is assisted by electron-phonon interactions.[57] However, such features are not observed by FTIR and signature resonances in Raman scattering spectra are no different in p-Si-NWs and n^+-Si NW, which do not exhibit any clear SiO_x presence, nor polyatomic Si-based $<500\ cm^{-1}$.

In electroluminescent device applications, the lack of an appreciable oxide is beneficial, since tunneling conduction and high voltage oxide breakdown issues are avoided in a spatially predefined mesoporous nanocrystal matrix in each NW.[58] For (electro)luminescent devices, particularly packaged devices, the influence of temperature on the nature and stability of the PL is important. Figure 8a shows the temperature dependent PL spectra for n^+- Si NWs and spectra from p- from 300–100 K are shown in Fig. 8b.

The FWHM remains constant over the temperature range for both types of NW. The temperature is limited to 100 K before the onset of reductions due to phonon-assisted low(er) temperature recombination or photo-generated carriers,[34] or by dominant Auger recombination processes. The spectra are very consistent, and do not exhibit luminescence bands that are affected by surface plasmon resonances of remnant Ag nanoparticles because of their effective removal after etching.

The PL spectra for both n^+- and p-Si NWs (Figs 8a and 8b) show consistent PL emission at energies greater than the effective quantum confined emission bandgap, and a marked increase in emission energy as the temperature is reduced. The bandgap remains an indirect one although excitons are confined and emission is intense. The variation of a bandgap in Fig. 9a that are 0.58 eV (p-Si NW) and 0.68 eV (n^+-Si NW) greater than the room temperature bandgap, varies similarly to the temperature variation of the bulk silicon bandgap from electron-phonon interactions as

$$E_{g,qc} = E_{g,qc}(0) - (\alpha T^2/T + \beta)$$

that shifts both conduction and valence bands, for both types of NWs. The extrapolated values of 1.92 eV and 1.77 eV at 0 K are unlikely to be approached due to phonon-assisted recombination at T < 100 K. Interestingly, the nanocrystal-decorated solid-core p-Si NWs exhibit the higher emission energies, and the emission energy lowers with increasing temperature at twice the rate of mesoporous wires. At higher temperatures, linear decrease is observed consistent with thermal lattice expansion modifications to the band structure, which plausibly is more likely in solid-core crystalline p-Si NWs. Additionally, as shown in Fig. 9b, the intensity of p-Si NW PL is lower by a factor of 2 – 2.5×, compared to the mesoporous n^+-Si NWs. The surface-bound nanocrystals on p-Si NW are attached to the central NW core, although with defined grain boundaries and different orientation with respect to the longitudinal axis of the parent NW. In spite of an oxide with a sub-stoichiometric composition at the interface and a stoichiometric SiO_2 outer region, carrier diffusion back to the bulk is less likely to influence the PL intensity compared to the density of nanocrystal emitters on the NW surfaces.

Both mesoporous (n^+) and nanocrystal-decorated (p) NWs exhibit greater intensity of emission at lower temperatures across the

Downloaded on 2015-09-01 to IP 93.94.208.154 address. Redistribution subject to ECS terms of use (see ecsdl.org/site/terms_use) unless CC License in place (see abstract).

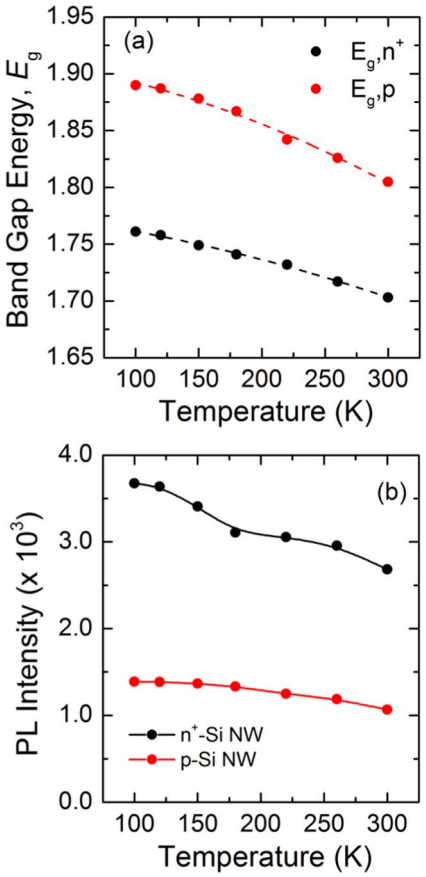


Figure 9. (a) Effective bandgap from the PL emission maximum for p-Si NWs and n$^+$-Si NWs from spectra acquired in the temperature range 100–300 K. (b) Variation of PL intensity acquired from the emission maximum at each temperature for both NW types.

broadband emission spectrum. Typically, it has be observed the PL intensity decreases with temperature when monitored at the effective bandgap energy, and explained via competing radiative and non-radiative decay rates and efficiency. In situations where a decrease with lower temperature is observed, the explanations have invoked single and triplet state mechanisms caused by electron-hole exchange interactions that split excitonic levels, with the latter, akin to phosphorescence, having a low probability but longer lifetime transition such that the singlet state emission rate is greater with temperature, and consequently, the intensity would decrease. Our measurements of the full PL spectrum at each temperature showed features similar to most direct bandgap semiconductors, with more intense PL observed at lower temperature.[59] In Fig. 9b, the full spectrum was acquired after equilibration at each temperature, and for nanocrystal-decorated p-Si NWs, the increase tends to a plateau (to 100 K) but increases monotonically with decreasing temperature for mesoporous n$^+$-Si NWs.

The fwhm, summarized in Fig. 10a shows a consistent increase in the broadband emission range with lower temperature for both NW types, with mesoporous NW showing the widest emission range at room temperature. Figure 10b shows the intensity variation with $1/kT$ according to

$$I\ (T) = I_0 \exp\left(\Delta E/kT\right)$$

yielding very low activation energies of 38.0 meV and 20.7 meV for p- and n$^+$-Si NWs respectively.

The observation that intense light emission emanates from quantum confinement from the nanocrystalline sub-structure of NWs, and the PL emission characteristics are specific to the nature of the nanocrystalline content of surface decorated p-Si NWs and internally mesoporous n$^+$-Si NWs, we now relate the emission characteristics

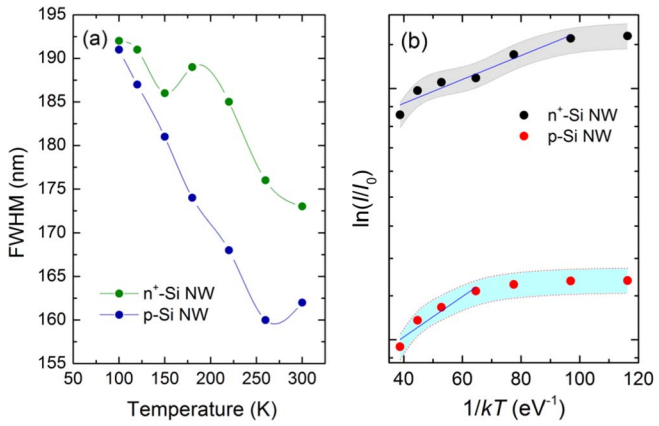


Figure 10. (a) FWHM of the PL spectra for n$^+$- and p-Si NWs acquired at temperatures in the range 100–300 K. The lines are guides to the eye. (b) Variation of the PL intensity with $1/kT$. The shaded regions are error bars.

to the size and size distribution of these emitters. Previous empirical correlations have related colloidal Si NC emission energy to the NC size via microscopy analysis. For Si NWs, particularly when the surface and internal structure act as NCs in terms of light emission, a relationship between peak effective bandgap emission is found with the nanocrystalline features on each NW. The PL linewidth is thus considered as the weighted sum of a statistical collection of individual quantum wires with bandgaps dependent on the inverse square of the crystallite length. Assuming that the probability of emission is independent of crystal size (for Si capable of visible luminescence), previous reports on the nanocrystal size contribution $D(E)$ to broadband PL emission have invoked a general mode that follows

$$\alpha D(E)^{-\gamma} = \left(E_g^p - E_g^{bulk}\right),$$

where $\gamma \rightarrow 1$ for realistic models incorporating effective masses of crystals that have no aspect ratio,[60] quantum dots as opposed to quantum dashes or wires. Our PL spectra are certainly broadened, and somewhat inhomogeneously into the lower energy tail.[61]

Finally, Fig. 11 shows the fitting of both room temperature PL spectra for p- and n$^+$-Si NWs. While the PL emission envelope in

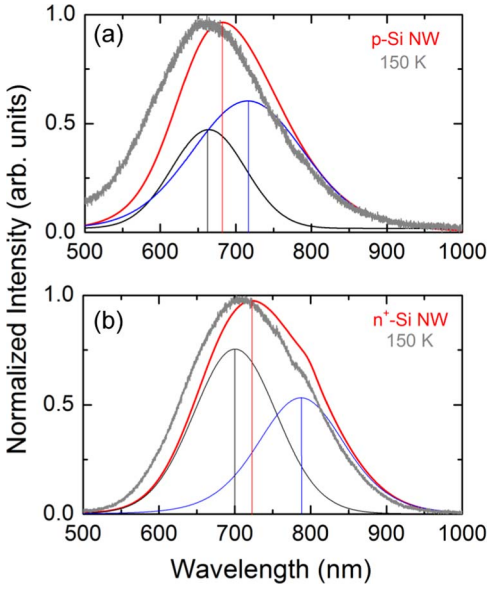


Figure 11. Normalized room temperature PL spectra deconvoluted using nanocrystal size distributions for (a) p-Si NWs and (b) n$^+$-Si NWs. Peak maxima are indicated with vertical lines. The normalized PL spectra acquired at 150 K are overlaid for each system.

Downloaded on 2015-09-01 to IP 93.94.208.154 address. Redistribution subject to ECS terms of use (see ecsdl.org/site/terms_use) unless CC License in place (see abstract).

some previous reports was fit with a range of 4–5 size contributions, the dominant emission for the n^+-Si NWs comprises a random, equi-spaced nanocrystal ensemble (confirmed from HRTEM analysis such as in Fig. 1) best fit with a pair of Gaussian distributions for quantum confined emitters. From nanocrystal-coated p-Si NWs in Fig. 11b, the PL emission profile at RT comprises two emission energies of 1.88 and 1.73 eV (p-type) and 1.77 and 1.57 eV (n^+-type). The temperature-dependent PL spectra in Fig. 8 by comparison, evolve with greater intensity blue emission while the RHS of the emission profile (sub-bandgap energies) remains relatively constant, i.e. the entire emission profile does not blueshift with lower temperature and the final emission energies are consistent with the higher energy emission band (super-bandgap energies) at RT that contributes to the overall PL form p-Si NWs and n^+-Si NWs.

In Figs. 11a, 11b, the bluer emission becomes more dominant at the expense of the lower energy emission, mimicking the (overlaid) 150 K PL profile. For rough, nanocrystal-decorated p-Si NWs with a two phase oxide coating (SiO_x at the interface and an outer SiO_2 layer), the increase in the super bandgap energy is pronounced with decreasing temperature. The nanocrystal mesoporous structure in n^+-Si NWs even at RT, shows a dominant emission from the smaller nanocrystals (Fig. 11b) at all temperatures.

The fwhm of the PL bands in p- and n^+-Si NWs (cf. Fig. 4) are ~0.39 and 0.42 eV respectively, confirming broadening of excitonic emission from more than one crystallite size. These estimates assumed that each size distribution produced equally efficient PL. The estimated nanocrystal size on the surface of p-Si NWs and the consistent crystalline sub-structure within the mesoporous n^+-Si NWs are both less than the excitonic Bohr radius of ~4.8 nm calculated from (100) crystal using equivalent electron and hole masses at RT. The localized centers in the form of nanocrystal surface protrusions on the p-Si NW surface act as nanocrystals that localize or confine *e-h* pairs and results in PL emission. The surface of a deformed quantum wire was previously shown to have a very rich surface electronic structure[62] that came from the surface topology. Sivakov et al.[63] separately showed that protrusion from the surface could be correlated to PL measurements.

Conclusions

In conclusion, we have shown the monolithic arrays of high density NWs formed on silicon result in NW-specific morphologies that influence their luminescent properties. High resistivity, p-type Si with a majority hole concentration, etches to produce thinner NWs with a defined surface roughness, whereas more conductive electron conducting n^+-Si NWs form internally mesoporous structures comprising a random internal network of nanocrystals. Each NW layer emits red light at room temperature, with mesoporous NW arrays showing intense red light photoluminescence visible with the naked eye. The data confirm that the emission is similar to that of Si nanocrystals, indicating quantum confinement effects cause the light emission processes. Importantly the work shows how the structure of the NWs themselves approximates two different nanocrystal systems, as the NWs themselves are too large to cause exciton confinement, and it explains the peculiarity of previous Raman scattering estimates of quantum confined nanocrystal size compared to the relatively large NW. Mesoporous NWs contain nanocrystals throughout their structure, while rough NWs are shown to be decorated with nanoscale crystallites of silicon, and emit with slightly higher energy red light with considerably lower intensity under identical pump illumination.

Bandgap modification in low thermal conductance materials, changes in resistance for electron and phonon specific heat alterations, sensing via capacitance owing to their influence to back-gate biasing condition, and their ability to emit intense red light makes Si monolithic NW arrays of either type of NW morphology useful for applications. Lastly, it should be possible to incorporate these in luminescent, electroluminescent and photonic devices in monolithic array formats as stable and efficient red light sources. For electroluminescent devices, further work may provide routes to achieve nanoscale p-n junctions, and multi-pass gain via the fast direct band excitonic recombination, instead of the typically and dominant slower indirect gap recombination that, as shown here, still has a long lifetime. Control over the coverage and stoichiometry and conformal thickness of the oxide will be important and a fuller understanding of the marked PL increase with time is needed. Growth of each type of NW is possible on wafer scale areas as Si-based light sources, with the caveat that the etched wafer area influences the etch depth. Such approaches are amenable to further processing and encapsulation, and given the high surface area and hierarchical length scale of the silicon crystal wires and arrays, they may also be suitable to sensors where surface functionalization by adsorbates can influence optical emission, particularly where emission is definitively from outer surface-bound nanoscale crystallites.

Acknowledgments

WMS acknowledges support under the framework of the INSPIRE programme, funded by the Irish Government's Programme for Research in Third Level Institutions, Cycle 4, National Development Plan 2007–2013. We thank Science Foundation Ireland and the Irish Research Council for financial support. The authors thank V. N. N. Mogili for assistance with bright field STEM measurements.

References

1. G. S. Armatas and M. G. Kanatzidis, *Science*, **313**, 817 (2006).
2. B. Kiraly, S. Yang, and T. J. Huang, *Nanotechnology*, **24**, 245704 (2013).
3. A. I. Hochbaum, D. Gargas, Y. J. Hwang, and P. Yang, *Nano Lett.*, **9**, 3550 (2009).
4. A. I. Hochbaum, R. Chen, R. D. Delgado, W. Liang, E. C. Garnett, M. Najarian, A. Majumdar, and P. Yang, *Nature*, **451**, 163 (2008).
5. Y. Qu, L. Liao, Y. Li, H. Zhang, Y. Huang, and X. Duan, *Nano Lett.*, **9**, 4539 (2009).
6. A. I. Boukai, Y. Bunimovich, J. Tahir-Kheli, J.-K. Yu, W. A. Goddard Iii, and J. R. Heath, *Nature*, **451**, 168 (2008).
7. I. Ponomareva, D. Srivastava, and M. Menon, *Nano Lett.*, **7**, 1155 (2007).
8. M. G. Ghossoub, K. V. Valavala, M. Seong, B. Azeredo, K. Hsu, J. S. Sadhu, P. K. Singh, and S. Sinha, *Nano Lett.*, **13**, 1564 (2013).
9. J. Lim, K. Hippalgaonkar, S. C. Andrews, A. Majumdar, and P. Yang, *Nano Lett.*, **12**, 2475 (2012).
10. B. Tian, X. Zheng, T. J. Kempa, Y. Fang, N. Yu, G. Yu, J. Huang, and C. M. Lieber, *Nature*, **449**, 885 (2007).
11. K. Q. Peng, Y. Xu, Y. Wu, Y. J. Yan, S. T. Lee, and J. Zhu, *Small*, **1**, 1062 (2005).
12. M. C. Hanna and A. J. Nozik, *J. Appl. Phys.*, **100**, 074510/1 (2006).
13. M. C. Beard, K. P. Knutsen, P. Yu, J. M. Luther, Q. Song, W. K. Metzger, R. J. Ellingson, and A. J. Nozik, *Nano Lett.*, **7**, 2506 (2007).
14. W. McSweeney, H. Geaney, and C. O'Dwyer, *Nano Res.*, **8**, 1395 (2015).
15. M. T. McDowell, S. W. Lee, W. D. Nix, and Y. Cui, *Adv. Mater.*, **25**, 4966 (2013).
16. C. K. Chan, H. Peng, G. Liu, K. McIlwrath, X. F. Zhang, R. A. Huggins, and Y. Cui, *Nat. Nanotechnol.*, **3**, 31 (2008).
17. S. Hu, M. R. Shaner, J. A. Beardslee, M. Lichterman, B. S. Brunschwig, and N. S. Lewis, *Science*, **344**, 1005 (2014).
18. G. Franzò, A. Irrera, E. C. Moreira, M. Miritello, F. Iacona, D. Sanfilippo, G. D. Stefano, P. G. Fallica, and F. Priolo, *Appl. Phys., A Mater. Sci. Process.*, **74**, 1 (2002).
19. L. Pavesi, L. D. Negro, C. Mazzoleni, G. Franzo, and F. Priolo, *Nature*, **408**, 440 (2000).
20. L. D. Negro, M. Cazzanelli, L. Pavesi, S. Ossicini, D. Pacifici, G. Franzo, F. Priolo, and F. Iacona, *Appl. Phys. Lett.*, **82**, 4636 (2003).
21. V. A. Belyakov, V. A. Burdov, R. Lockwood, and A. Meldrum, *Adv. Opt. Technol.*, 279502 (2008).
22. M. P. Stewart and J. M. Buriak, *Adv. Mater.*, **12**, 859 (2000).
23. V. S.-Y. Lin, K. Motesharei, K.-P. S. Dancil, M. J. Sailor, and M. R. Ghadiri, *Science*, **278**, 840 (1997).
24. L. T. Canham, *Appl. Phys. Lett.*, **57**, 1046 (1990).
25. V. Lehman, *Electrochemistry of Silicon*, Wiley-VCH, Weinheim, Germany (2002).
26. A. G. Cullis and L. T. Canham, *Nature*, **353**, 335 (1991).
27. V. Schmidt, H. Riel, S. Senz, S. Karg, W. Riess, and U. Gösele, *Small*, **2**, 85 (2006).
28. J. Goldberger, A. I. Hochbaum, R. Fan, and P. Yang, *Nano Lett.*, **6**, 973 (2006).
29. R. D. Kekatpure and M. L. Brongersma, *Phys. Rev. A*, **78**, 023829 (2008).
30. R. D. Kekatpure and M. L. Brongersma, *Nano Lett.*, **8**, 3787 (2008).
31. W.-Q. Huang, S.-R. Liu, C.-J. Qin, Q. Lü, and L. Xu, *Opt. Commun.*, **284**, 1992 (2011).
32. M. I. J. Beale, J. D. Benjamin, M. J. Uren, N. G. Chew, and A. G. Cullis, *J. Cryst. Growth*, **73**, 622 (1985).
33. R. L. Smith and S. D. Collins, *J. Appl. Phys.*, **71**, R1 (1992).
34. O. Demichel, V. Calvo, N. Pauc, A. Besson, P. Noé, F. Oehler, P. Gentile, and N. Magnea, *Nano Lett.*, **9**, 2575 (2009).
35. B. J. Kim, J. Tersoff, S. Kodambaka, M. C. Reuter, E. A. Stach, and F. M. Ross, *Science*, **322**, 1070 (2008).

Downloaded on 2015-09-01 to IP 93.94.208.154 address. Redistribution subject to ECS terms of use (see ecsdl.org/site/terms_use) unless CC License in place (see abstract).

36. V. Schmidt, S. Senz, and U. Gösele, *Nano Lett.*, **5**, 931 (2005).
37. J. Valenta, B. Bruhn, and J. Linnros, *Nano Lett.*, **11**, 3003 (2011).
38. N. Geyer, Z. Huang, B. Fuhrmann, S. Grimm, M. Reiche, T.-K. Nguyen-Duc, J. d. Boor, H. S. Leipner, P. Werner, and U. Gosele, *Nano Lett.*, **9**, 3106 (2009).
39. K. Q. Peng, Y. Wu, H. Fang, X. Y. Zhong, Y. Xu, and J. Zhu, *Angew. Chem. Int. Ed.*, **44**, 2737 (2005).
40. X. Zhong, Y. Qu, Y.-C. Lin, L. Liao, and X. Duan, *ACS Appl. Mater. Interfaces*, **3**, 261 (2011).
41. C. Chartier, S. Bastide, and C. Lévy-Clément, *Electrochim. Acta*, **53**, 5509 (2008).
42. W. McSweeney, O. Lotty, N. Mogili, C. Glynn, H. Geaney, D. Tanner, J. Holmes, and C. O'Dwyer, *J. Appl. Phys.*, **114**, 034309 (2013).
43. K. Balasundaram, J. S. Sadhu, J. C. Shin, B. Azeredo, D. Chanda, M. Malik, K. Hsu, J. A. Rogers, P. Ferreira, S. Sinha, and X. Li, *Nanotechnology*, **23**, 305304 (2012).
44. X. Zhong, Y. Qu, Y.-C. Lin, L. Liao, and X. Duan, *ACS Appl. Mater. Interfaces*, **3**, 261 (2011).
45. A. Hochbaum and P. D. Yang, *Chem. Rev.*, **110**, 527 (2010).
46. Y. Qu, H. Zhou, and X. Duan, *Nanoscale*, **3**, 4060 (2011).
47. E. Quiroga-González, J. Carstensen, C. Glynn, C. O'Dwyer, and H. Föll, *Phys. Chem. Chem. Phys.*, **16**, 255 (2014).
48. C. O'Dwyer, D. N. Buckley, D. Sutton, and S. B. Newcomb, *J. Electrochem. Soc.*, **153**, G1039 (2006).
49. H. Föll, S. Langa, J. Carstensen, M. Christophersen, and I. M. Tiginyanu, *Adv. Mater.*, **15**, 183 (2003).
50. W. McSweeney, C. Glynn, H. Geaney, G. Collins, J. D. Holmes, and C. O'Dwyer, *Semicon. Sci. Technol.* (2015).
51. P. Artoni, A. Irrera, F. Iacona, E. F. Pecora, G. Franzò, and F. Priolo, *Opt. Express*, **20**, 1483 (2012).
52. J. P. Feser, J. S. Sadhu, B. P. Azeredo, K. H. Hsu, J. Ma, J. Kim, M. Seong, N. X. Fang, X. Li, P. M. Ferreira, S. Sinha, and D. G. Cahill, *J. Appl. Phys.*, **112**, 114306 (2012).
53. J. Fuzell, A. Thibert, T. M. Atkins, M. Dasog, E. Busby, J. G. C. Veinot, S. M. Kauzlarich, and D. S. Larsen, *J. Phys. Chem. Lett.*, **4**, 3806 (2013).
54. R. Ghosh, P. K. Giri, K. Imakita, and M. Fujii, *Nanotechnology*, **25**, 045703 (2014).
55. L. Tsybeskov, J. V. Vandyshev, and P. M. Fauchet, *Phys. Rev. B*, **49**, 7821 (1994).
56. J. H. Kim, H. H. An, and C. S. Yoon, *J. Appl. Phys.*, **105**, 076102 (2009).
57. J. L. Gole and D. A. Dixon, *J. Phys. Chem. B*, **102**, 33 (1998).
58. A. Irrera, P. Artoni, F. Iacona, E. F. Pecora, G. Franzò, M. Galli, B. Fazio, S. Boninelli, and F. Priolo, *Nanotechnology*, **23**, 075204 (2012).
59. A. M. Hartel, S. Gutsch, D. Hiller, and M. Zacharias, *Phys. Rev. B*, **85**, 165306 (2012).
60. J. Valenta, B. Bruhn, and J. Linnros, *Nano Lett.*, **11**, 3003 (2011).
61. D. Yao, G. Zhang, and B. Li, *Nano Lett.*, **8**, 4557 (2008).
62. G. Cantele, D. Ninno, and G. Iadonisi, *Phys. Rev. B*, **61**, 13730 (2002).
63. V. A. Sivakov, F. Voigt, A. Berger, G. Bauer, and S. H. Christiansen, *Phys. Rev. B*, **82**, 125446 (2010).

Downloaded on 2015-09-01 to IP **93.94.208.154** address. Redistribution subject to ECS terms of use (see **ecsdl.org/site/terms_use**) unless CC License in place (see abstract).